

Radio Relics Tracing the Projected Mass Distribution in CIZA J2242.8+5301 *

N. OKABE,^{1,2,3} H. AKAMATSU,⁴ J. KAKUWA,¹ Y. FUJITA,⁵ Y. -Y. ZHANG,⁶ M. TANAKA,⁷ and K. UMETSU,⁸

¹*Department of Physical Science, Hiroshima University, 1-3-1 Kagamiyama, Higashi-Hiroshima, Hiroshima 739-8526, Japan*

²*Hiroshima Astrophysical Science Center, Hiroshima University, Higashi-Hiroshima, Kagamiyama 1-3-1, 739-8526, Japan*

³*Kavli Institute for the Physics and Mathematics of the Universe (WPI), Todai Institutes for Advanced Study, University of Tokyo, 5-1-5 Kashiwanoha, Kashiwa, Chiba 277-8583, Japan*

okabe@hiroshima-u.ac.jp

⁴*SRON Netherlands Institute for Space Research, Sorbonnelaan 2, 3584 CA Utrecht, The Netherlands*

⁵*Institute of Space and Astronautical Science, Japan Aerospace Exploration Agency, 3-1-1 Yoshinodai, Chuo-ku, Sagami-hara, Kanagawa 229-8510, Japan*

⁶*Argelander-Institut für Astronomie, Universität Bonn, Auf dem Hügel 71, 53121 Bonn, Germany*

⁷*National Astronomical Observatory of Japan, Mitaka, Tokyo 181-8588, Japan*

⁸*Institute of Astronomy and Astrophysics, Academia Sinica, P.O. Box 23-141, Taipei 10617, Taiwan*

(Received (reception date); accepted (acceptation date))

Abstract

We present a weak-lensing analysis for the merging galaxy cluster, CIZA J2242.8+5301, hosting double radio relics, using three-band Subaru/Suprime-Cam imaging ($Br'z'$). Since the lifetime of dark matter halos colliding into clusters is longer than that of X-ray emitting gas halos, weak-lensing analysis is a powerful method to constrain a merger dynamics. Two-dimensional shear fitting using a clean background catalog suggests that the cluster undergoes a merger with a mass ratio of about 2:1. The main halo is located around the gas core in the southern region, while no concentrated gas core is associated with the northern sub halo. We find that the projected cluster mass distribution resulting from an unequal-mass merger is in excellent agreement with the curved shapes of the two radio relics and the overall X-ray morphology except for the lack of the northern gas core. The lack of a prominent radio halo enables us to constrain an upper limit of the fractional energy of magneto-hydrodynamics turbulence of $(\delta B/B)^2 < \mathcal{O}(10^{-6})$ at a resonant wavenumber, by a balance between the acceleration time and the time after the core passage or the cooling time, with an assumption of resonant acceleration by second-order Fermi process.

Key words: galaxies: clusters: individual (CIZA J2242.8+5301) - gravitational lensing: weak - X-rays: galaxies: clusters

1. Introduction

The acceleration mechanism generating relativistic particles in the intracluster medium (ICM) along with its associated non-thermal phenomena is one of the long-standing unresolved problems in studies of cluster physics. The presence of relativistic electrons and magnetic fields is recognized by diffuse, synchrotron radio emission (on Mpc scales), which is not associated with compact sources such as AGN, but with cluster merging (e.g. Feretti et al. 2012; Brunetti & Jones 2014). The diffuse radio emission in galaxy clusters is classified according to their morphology into two types, radio halos and relics. Radio halos, to first order, follow the X-ray brightness distribution in the central region, sometimes along with a curved spectrum (e.g. Brunetti et al. 2008). Radio relics display a filamentary structure in the peripheral region. Some relics have a harder spectrum than that of radio halos (e.g. Brunetti et al. 2008; van Weeren et al. 2010). The fundamental

physics to form radio halos and relics and give rise to different morphological types are one of the most outstanding problems. Furthermore, the acceleration mechanism is still unclear from the theoretical side. In theory, two types of acceleration mechanism have been proposed, the first (e.g. Bell 1978; Blandford & Ostriker 1978; Drury 1983) and second order Fermi acceleration (e.g. Schlickeiser et al. 1987; Ohno et al. 2002; Fujita et al. 2003; Brunetti et al. 2004). It is unresolved through what process relativistic particles are accelerated/re-accelerated in merging clusters. Since the merger dynamics is controlled by dark matter, it is of vital importance for understanding non-thermal phenomena to measure the cluster mass distribution for merging clusters. (e.g. Okabe & Umetsu 2008; Okabe et al. 2010, 2011; Medezinski et al. 2015).

Recent radio observation (van Weeren et al. 2010) discovered spectacular, double-giant radio relics in CIZA J2242.8+5301. The northern relic is larger than the southern one, which suggests non-equal-mass merger (van Weeren et al. 2011). The northern giant relic shows a spatial distribution of aging relativistic electrons, indicating a presence of strong magnetic field ($5 - 7 \mu\text{G}$). The

* Based on data collected at Subaru Telescope, which is operated by the National Astronomical Observatory of Japan.

magnetic field at the radio relic is stronger than equipartition magnetic fields in radio halos ($\sim 0.1 - 1\mu\text{G}$), but consistent with a lower limit of the magnetic field ($> 3\mu\text{G}$) in other relics by comparing the inverse Compton X-ray emission with the measured radio synchrotron emission (e.g. Nakazawa et al. 2009; Finoguenov et al. 2010). Assuming a diffusive shock acceleration (DSA; Drury 1983), the Mach number of shock velocity is expected to be $\mathcal{M} = 4.6_{-0.9}^{+1.3}$. *Suzaku* X-ray observation (Akamatsu & Kawahara 2013) has discovered a temperature jump across the northern relic and estimated that the Mach number is somewhat lower than expected by radio observation. A discrepancy between the X-ray-estimated and radio-estimated Mach numbers makes it puzzling to understand a particle acceleration process. On the other hand, Stroe et al. (2014) have pointed out that an intrinsic beam-image with of the radio telescope affects the estimation of the radio spectral index and revised $\mathcal{M} = 2.90_{-0.13}^{+0.10}$ which is close to X-ray measurements. Therefore, the study on a comparison of Mach numbers is still controversial. No prominent radio halo in the central region is found by multi-bands radio analysis (van Weeren et al. 2010; Stroe et al. 2013). Recent study of weak-lensing analysis (Jee et al. 2015) has shown a bimodal structure of the dark matter and member galaxies and concluded an equal-mass merger.

We here report weak-lensing analysis using data from Subaru/Suprime-Cam. The paper is organized as follows: Section 2 presents the weak-lensing analysis of Subaru/Suprime-Cam. We present distribution of member galaxies and mass measurements in Sections 3 and 4, respectively. In Section 5, we compare the projected mass distribution with the X-ray emitting gas, radio relics and member galaxy distribution. The results are discussed in Section 6 and summarized in Section 7. We use $\Omega_{m,0} = 0.3$, $\Omega_{\Lambda} = 0.7$ and $H_0 = 100h \text{ km s}^{-1} \text{ Mpc}^{-1}$ ($H_0 = 70h_{70} \text{ km s}^{-1} \text{ Mpc}^{-1}$).

2. Data Analysis

We took three-band imaging data (B, r', z') for CIZAJ2242.8+5301 ($z_l = 0.192$) with the Suprime-cam (Miyazaki et al. 2002) at the Subaru 8.2-m telescope. Here, the subscript l denotes the lensing (cluster) redshift. The exposure times for the B -, r' - and z' - bands are 24, 36 and 12 mins, respectively. Those imaging are taken through the Service program (P.I.:N. Okabe). The r' - image, of which seeing is 0.7 arcsec, is used to measure ellipticities of galaxies. The other bands are combined with the r' -band data to minimize a contamination of unlensed member galaxies in background source catalog.

We use the standard pipeline reduction software for the Suprime-Cam, SDFRED (Yagi et al. 2002; Ouchi et al. 2004) modified for the new CCDs. The data reduction follows Okabe et al. (2013, 2014a). The zero point of magnitude is corrected for the Galactic extinction (Schlafly & Finkbeiner 2011) using a single function over the whole field and calibrated by comparing magnitudes of stellar objects with those of standard stars

We measure ellipticity of each galaxy in terms of weighting the surface brightness, following the KSB method (Kaiser et al. 1995) with some modifications (Okabe et al. 2014a). The details are described in Okabe et al. (2014a). The photometric redshift of each galaxy is estimated as the ensemble average of the COSMOS photometric redshift (Ilbert et al. 2013) of neighboring COSMOS galaxies in the three-magnitudes plane. We adopt 100 COSMOS galaxies for the estimation and confirm that the change by changing the sampling number is negligible. The galaxies for shape measurements are selected by $r_h > \bar{r}_h^* + \delta r_h^*$, $r_g > \bar{r}_g^* + \delta r_g^*$ and $22 < r'$, where r_h and r_g are the half-light radius and the Gaussian radius, respectively. The asterisk denotes the stellar objects. Since the cluster is located at the Galactic plane, the number density of background galaxies is small 9 arcmin^{-2} because of a considerable number of contaminated stars, compared to those in previous studies (e.g. Okabe & Umetsu 2008; Okabe et al. 2010, 2013; Umetsu et al. 2014).

A secure background selection is critically important to measure accurately cluster and subcluster masses (e.g. Broadhurst et al. 2005; Okabe et al. 2013; Okabe & Smith 2015). We use color information ($r' - z'$ and $B - r'$) for the selection (e.g. Medezinski et al. 2010; Umetsu et al. 2010). The red-sequence of member E/S0 galaxies appeared in (r' and $r' - z'$) and (r' and $B - r'$) planes is fitted with a linear function. The mean lensing depth $\langle D_{ls}/D_s \rangle$ is computed as a function of the color offsets from the red-sequence of ($r' - z'$) - $(r' - z')_{\text{E/S0}}$ and ($B - r'$) - $(B - r')_{\text{E/S0}}$. Here, D_s and D_{ls} are the angular diameter distances to the sources and between the cluster (lens) and the sources, respectively. The resulting $\langle D_{ls}/D_s \rangle$ map is shown in the left panel of Figure 1. The grid box size is 0.1ABmag. $\langle D_{ls}/D_s \rangle$ at small color-offsets presents low lensing depth, suggesting a finite contamination of member galaxies. Following Medezinski et al. (2010), we first select galaxies of which $(B - r')$ is bluer than those of clusters ($(B - r') - (B - r')_{\text{E/S0}} < -\sigma_{B-r'}$), where $\sigma_{B-r'}$ is the color width of the red sequence. In a similar manner, galaxies of which colors are located in the width of $\sigma_{r'-z'}$ are excluded in our source background catalog. Since a combination of the lensing depth and the color information is a good estimator to monitor the color distribution for possible member galaxies, we exclude color regions for our background sources by employing $\langle D_{ls}/D_s \rangle < 0.6$, which is equivalent to $\langle z_s \rangle < 0.52$. The number density of background source galaxies is 2.6 arcmin^{-2} . The mean source redshift is $\langle z_s \rangle = 0.639$.

3. Galaxy Distribution

We make a map of member galaxies for visual purpose to depict the configuration of cluster merger. We here define bright member galaxies with $r' < 21\text{ABmag}$, $|(B - r') - (B - r')_{\text{E/S0}}| < \sigma_{B-r'}$ and $|(r' - z') - (r' - z')_{\text{E/S0}}| < \sigma_{r'-z'}$. The luminosity in the r' -band is computed with K-correction assuming a single cluster redshift. We make a luminosity map convolved with a Gaussian smoothing kernel $\propto \exp[-\theta^2/\theta_g^2]$, where $\theta_g = 2'$ corre-

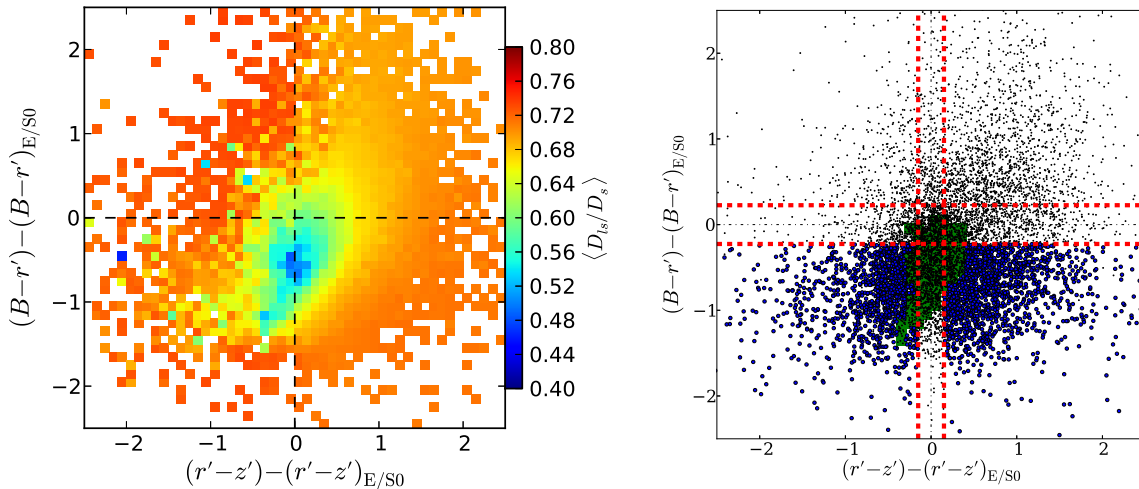


Fig. 1. Left : $\langle D_{ls}/D_s \rangle$ distribution in the color-offset plane of $(r' - z') - (r' - z')_{E/S0}$ and $(B - r') - (B - r')_{E/S0}$. Right: black points are all galaxies for which shapes are measured. Blue points are background galaxies. Green region denotes the color area with $\langle D_{ls}/D_s \rangle < 0.6$. Red dashed lines are the width of the red sequence.

sponding to $\text{FWHM} = 3'.3$. The right panel of Figure 2 clearly shows a bimodal structure of member galaxies. The luminosity peaks are associated with the brightest cluster galaxies for two halo components, which provides us with priors of the number of halos and their central positions.

4. Mass Measurement

We simultaneously fit a two-dimensional shear pattern with multi-components model, following previous papers (see details; Okabe et al. 2011; Watanabe et al. 2011; Merluzzi et al. 2015). We pixelize the shear pattern into a regular grid of $1' \times 1'$ without any spatial smoothing procedures. We employ the NFW mass model predicted by numerical simulations (Navarro et al. 1996) as the mass model. The NFW mass density profile is specified by two parameters of the mass M_Δ and the halo concentration c_Δ , where Δ denotes Δ times the critical mass density, $\rho_{\text{cr}}(z_l)$, at the cluster redshift. We also treat centers (α_c, δ_c) of the two mass components as free parameters (e.g. Oguri et al. 2010). Based on a prior of member galaxy distribution (Section 3; right panel of Figure 2), we consider two-halo components in the northern and southern region. There are eight parameters in total $\mathbf{p} = (M_\Delta^S, c_\Delta^S, M_\Delta^N, c_\Delta^N, \alpha_c^S, \delta_c^S, \alpha_c^N, \delta_c^N)$. Here, the superscripts denote the southern halo (S) and the northern halo (N), respectively. We adopt the Markov Chain Monte Carlo method with standard Metropolis-Hastings sampling. Since it is difficult to determine the concentration parameter of each individual halo because of the small number of background galaxies and the degeneracy between model parameters, we use a Gaussian prior that follows the halo concentration-mass (c - M) relation

of Bhattacharya et al. (2013) derived from N-body cosmological simulations. The Bhattacharya et al. (2013) c - M relation is in agreement with recent stacked lensing studies (Okabe et al. 2013; Okabe & Smith 2015; Umetsu et al. 2014, 2015). We use a flat prior for other parameters. The ranges of virial masses are restricted to $0 < M_\Delta < 30 \times 10^{14} h^{-1} M_\odot$. The centers are allowed within $\pm 2'$ around the candidates of most luminous cluster galaxies. The best-fit parameters are shown in Table 1. The best-fit mass for the southern halo is twice higher than that for the northern halo, though an equal-mass ratio cannot be ruled out within errors. The offsets between lensing centers and most luminous galaxies on the sky plane for the southern and the northern halos are $36_{-36}^{+118} h^{-1} \text{kpc}$ and $151_{-67}^{+233} h^{-1} \text{kpc}$, respectively. Thus, the offset is not significant for the southern main halo and at $\sim 2\sigma$ level for the northern subhalo.

The tangential shear profiles of two mass components as a function of the projected distance from the best-fit center of the southern halo are shown in Figure 3. The center is set to be the best-fit value. The lensing signal at $r \sim 8'$ is depressed by the northern mass halo. The best-fit lensing profile for the southern halo (green dashed line) monotonically decreases, while the best-fit lensing profile for the northern halo (blue dotted line) rapidly increases up at $r \sim 8'$ due to an off-centering effect (e.g. Yang et al. 2006). The total mass model (red solid line) well describes the observed lensing profile.

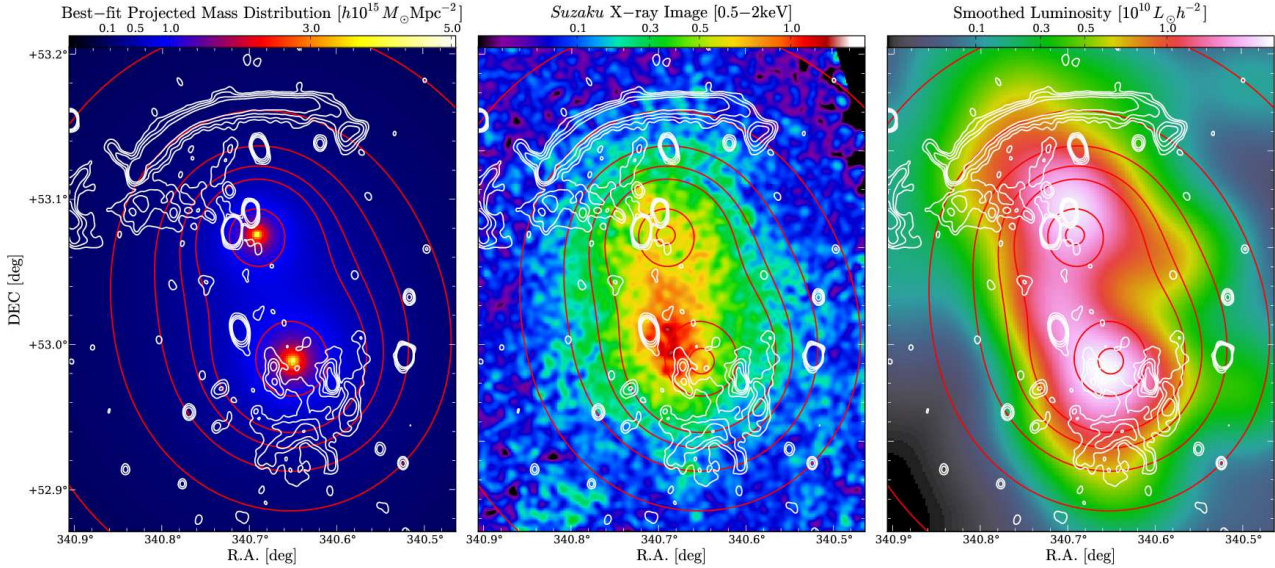


Fig. 2. Right: the best-fit mass distribution computed from a simultaneous fit of two-dimensional shear pattern (Sec 4). Contour (red) levels are in units of the convergence, κ , starting from $\kappa = 0.1$ with steps of $\kappa = 0.1$. Overlaid contours (white) are the radio emission (Stroe et al. 2013) at 1.2 GHz in units of signal-to-noise ratio $[4, 8, 16, 32]\sigma_{\text{RMS}}$. Middle: X-ray image of *Suzaku* satellite in 0.5 – 2.0keV (Akamatsu & Kawahara 2013; Akamatsu et al. 2015). Right : Luminosity map for bright member galaxies (Sec 3) computed with Gaussian smoothing FWHM= 3/3.

Table 1. Mass estimates for the southern and northern mass components ($10^{14} h^{-1} M_{\odot}$) and their centroids in the units of degree, respectively.

Δ	M_{Δ}^S	c_{Δ}^S	M_{Δ}^N	c_{Δ}^N	$(\alpha_c, \delta_c)^S$	$(\alpha_c, \delta_c)^N$
vir	$12.44^{+9.86}_{-6.58}$	$4.60^{+1.96}_{-1.28}$	$6.74^{+7.64}_{-4.12}$	$5.34^{+2.25}_{-1.61}$	$(340.651^{+0.028}_{-0.019}, 52.989^{+0.015}_{-0.016})$	$(340.692^{+0.020}_{-0.028}, 53.076^{+0.011}_{-0.014})$
200	$10.69^{+9.82}_{-5.67}$	$3.44^{+1.51}_{-0.98}$	$5.51^{+6.39}_{-3.43}$	$4.11^{+1.97}_{-1.26}$	$(340.651^{+0.028}_{-0.019}, 52.989^{+0.015}_{-0.016})$	$(340.692^{+0.020}_{-0.029}, 53.075^{+0.015}_{-0.012})$

5. A comparison between Projected Distributions of Radio Relic, ICM, and Mass

The acceleration process of relativistic electrons emitting giant relics are believed to be associated with on-going merger, but the details remain unknown. Since the dark matter controls the merger dynamics, a comparison of projected distributions between the dark matter, the gas and the radio relics would provide us with an important information for understanding the non-thermal physics (e.g. Okabe et al. 2010). Since the number density of background galaxies is small, we compute the projected mass distribution calculated from the best-fit parameters without any smoothing kernels, rather than weak-mass reconstruction (Okabe & Umetsu 2008) in order to avoid noisy feature. The best-fit projected mass distribution makes it clear to understand the configuration of cluster merger. We also investigate the projected mass distribution by changing parameters with 1σ measurement errors, the overall feature is not significantly changed. The resultant maps are shown in the left panel of Figure 2. The left panel is the best-fit mass distribution, overlaid with radio contours (Stroe et al. 2013). The more and less massive clusters are located at the south and the north, respec-

tively. Both the northern and the southern relics are very similar to the projected mass distribution. In particular, the curved shapes of two relics are tightly correlated with the curvature of the iso-contours of the projected mass distribution. It indicates that the bimodal mass distribution with a different mass ratio has some influence on the formation of asymmetric radio relics.

The middle panel compares the X-ray surface brightness distribution with the mass distribution and the radio relics. The X-ray distribution is elongated along the north-south direction. The overall gas distribution is in an excellent agreement with the mass distribution. Especially, the faint X-ray emission (green color) at $\sim 5'$ from the merger axis follows the curvature of dark matter distribution. The X-ray peak is associated with the southern massive cluster, while no prominent gas core is found around the center of the northern less massive cluster. It suggests that the gas core associated with the northern subcluster is disrupted by the merger (Tormen et al. 2004).

The smoothed luminosity map for member galaxies (right panel; Sec. 3) shows a clear bimodal spatial distribution which is similar to weak-lensing mass distribution. The luminosity around each central region is comparable to each other. We compute the mass-to-

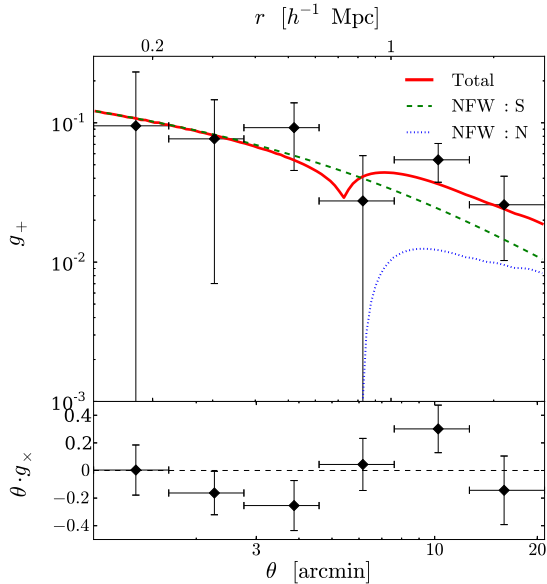


Fig. 3. Top panel : tangential shear profile as a function of the projected cluster-centric radius from the center of the southern main halo determined by two-dimensional shear fitting. A bump in the profile signals is found at $r \gtrsim 8'$. The profile is well described by two NFW components of the northern and southern halos. The red solid, green dashed and blue dotted lines are the best-fitting NFW profile for the two halos, the southern halo and the northern halo, respectively. Bottom panel: the 45° rotation components, $\theta \cdot g_x$.

light ratio within $< 250h_{70}^{-1}$ with central positions determined by two-dimensional shear pattern. We obtain $M/L(< 250h_{70}^{-1}) = 687 \pm 245h_{70}M_\odot/L_\odot$ for the southern halo and $429 \pm 184h_{70}M_\odot/L_\odot$ for the northern halo, respectively. Here, we use the projected mass for each halo component and the r -band total luminosity corrected with a Schechter luminosity function in the central region ($< 500h_{70}^{-1}$; Popesso et al. 2005). The mass-to-light ratio is somewhat larger than those in other clusters (e.g. Okabe & Umetsu 2008; Medezinski et al. 2010). This could be caused by the fact that some member galaxies are missing due to a contamination of a considerably number of stars in Galactic-plane position. Although the viral mass for the southern halo is about two times higher than that for the northern halo, the mass-to-light ratios are comparable because two masses within small radii are comparable due to a difference of the concentration parameter (Table 1).

6. Discussion

The best-fit parameters obtained by two-dimensional shear fitting suggest that CIZAJ2242.8+5301 undergoes the cluster merger with $\sim 2:1$ mass ratio. The main cluster is the southern halo and the subcluster is the northern halo, respectively. The overall distribution of X-ray emitting gas is similar to the projected mass distribution (the middle panel in Figure 2). On the other hand, the gas core is associated with the main cluster, while no sig-

nificant gas core around the northern subhalo is found. It indicates that the gas core associated with the main cluster survives under the collisional matter interaction and the gas core with the subhalo is disrupted (Tormen et al. 2004). *Chandra* X-ray observation (Ogreaan et al. 2014) has reported possible density jumps in the surface brightness profile at inner radii between two relics. Visual inspection of their result suggests that those jumps follow the overall mass distribution. The *Chandra* X-ray image also shows that the X-ray emission from the northern central region (at $r \sim 2'$ from from the approximate northern subhalo center) is somewhat more extended than that from the southern central region. It would point out that the disrupted gas core in the subhalo is more extended. Although the gas distribution does not always follow the dark matter distribution in violent merging clusters (Okabe & Umetsu 2008), the gas distribution is similar to the dark matter distribution in the cluster on a very early stage after the core passage. The big giant radio relic is in the front of an advancing direction of the northern subhalo. Asymmetric radio relics are very similar to the projected mass distribution.

Since the dark matter subhalo is less disrupted by the cluster merger compared to the collisional gas core, the positions of dark matter halos provide us with the fundamental information of the cluster merger. The distance between weak-lensing determined centers of two halos is $\sim 712 h^{-1}\text{kpc}$. The center of mass can be estimated to be $(340.667\text{deg}, 53.0202\text{deg})$ assuming a point mass. The distances between outer edge of the northern relic and the center of mass, $d_{\text{NR-CM}}$, and between outer edge of the southern relic and the center of mass, $d_{\text{SR-CM}}$ are $\sim 9'$ and $\sim 5.4'$, respectively. Interestingly, the distance ratio is approximately equal to the ratio of the Mach numbers estimated by X-ray temperature, $d_{\text{NR-CM}} : d_{\text{SR-CM}} \sim \mathcal{M}_{\text{NR}} : \mathcal{M}_{\text{SR}}$ (Akamatsu et al. 2015), where $\mathcal{M}_{\text{NR}} = 2.7_{-0.4}^{+0.7}$ and $\mathcal{M}_{\text{SR}} = 1.7_{-0.3}^{+0.4}$. Furthermore, the projected distances between the dark matter halos and the center of the mass, $d_{\text{NM-CM}}$ and $d_{\text{SM-CM}}$, follow this ratio $d_{\text{NM-CM}} : d_{\text{SM-CM}} \sim \mathcal{M}_{\text{NR}} : \mathcal{M}_{\text{SR}}$. Since the distance is equivalent to the merger timescale multiplied by the velocity, those positions relative to the center of mass are simply explained by the timescale after the core passage. In other words, the formation of radio relic is possibly triggered after the core passage. Our mass measurement could consistently explain the merger configuration observed by X-ray, radio and weak-lensing techniques.

The particle acceleration mechanism of relativistic electrons is one of the unsettled problems. A visual inspection of the sharp morphology of radio relics (e.g. Brunetti & Jones 2014) and the spectral aging (van Weeren et al. 2010) suggest that radio relics are connected with merger shocks. Indeed, X-ray observations (Akamatsu & Kawahara 2013; Akamatsu et al. 2015) discovered the temperature jump around the radio relics, though the Mach numbers estimated by X-ray observation ($\mathcal{M}_{\text{NR}} = 2.7 \pm 0.5$ and $\mathcal{M}_{\text{SR}} = 1.7 \pm 0.3$) are somewhat lower than those ($\mathcal{M}_{\text{NR}} = 4.58 \pm 1.09$ and $\mathcal{M}_{\text{SR}} = 2.81 \pm 0.19$) by radio spectral index based on DSA model

(Stroe et al. 2013). Stroe et al. (2014) have revised $\mathcal{M}_{\text{NR}} = 2.90^{+0.10}_{-0.13}$ by considering a convolution of the beam size of radio telescopes. Weak-lensing analysis has shown that the morphology of radio relics is similar to the projected mass distribution. It indicates that the shapes of radio relics on the cluster scale radio relics well follow the global structure of the mass distribution. The observational fact implies the connection between the gas physics and the dark matter distribution. Two scenarios of the formation of radio relic are proposed. First, van Weeren et al. (2010) have suggested that a cluster merger shock accelerates electrons through some processes like the DSA (Drury 1983). Second, the fossil radio plasma seeded in the past (e.g. radio lobes from active galactic nuclei) is re-accelerated by gas compression or shocks (e.g. Enßlin & Gopal-Krishna 2001; Hoeft et al. 2004; Markevitch et al. 2005). Hoeft et al. (2004) have shown by numerical simulations that the radio ghost is flared at curved merger shocks. Although this study cannot constrain the formation process of radio relics, it is worth mentioning that the second scenario should be discussed in the cluster community, because the first scenario conflicts with other observational evidences but the second does not. Prominent detached shocks in A520 and the bullet cluster which have been first discovered by X-ray observations are not associated with radio relics but with radio halos (Govoni et al. 2004). If all merger shocks injected relativistic electrons, the radio relic should be observed in other famous merging clusters. If the formation of radio relic depends on the initial fossil radio plasma, we do not face the above problem. In order to understand the formation of radio relics, further systematic multi-wavelength studies of X-ray, radio, optical and weak-lensing analyses are vitally important.

We compare with previous numerical simulations regarding cluster mergers. van Weeren et al. (2011) have conducted numerical simulations for the cluster and shown that the northern massive cluster with the largest X-ray core radius triggers the largest shock wave after the core passage. Their result conflicts with both X-ray and weak-lensing measurements, because the X-ray gas core is not in the north region and the massive subhalo is located in the south region. Some discrepancy between the results of simulations and observations would be caused by a choice of their initial conditions. For instance, they assumed that the gas temperature is almost isothermal, while recent studies (Okabe et al. 2014b) pointed out that the gas temperature universally drops off beyond $\sim 0.5r_{200}$. The intrinsic scatter of the gas density deviated from the universal profile (Okabe et al. 2014b) might be also important. The observed configuration of the radio relics and X-ray surface brightness distributions are realized by other numerical simulations (Loken et al. 1995; Roettiger et al. 1999). A head-on merger with a mass ratio of 1:4 in less than 1Gyr after core passage (Loken et al. 1995) have shown that the largest gas core and the prominent shock are found in the more and less massive halos, respectively. Roettiger et al. (1999) have conducted the magneto-hydrodynamics (MHD) and dark matter simu-

lation to study A3667 and shown that a cluster merger of a mass ratio of 1:5 reproduce a largest radio relic associated with a subhalo and X-ray emission associated with a main halo. The mass ratios in two simulations are somewhat larger than that for the cluster. Those simulations assumed the first order Fermi acceleration to compute the radio relics. In order to precisely realize the observed features by numerical simulations, further studies using observational results would be important to understand the formation of radio relics. Cosmological MHD simulations (Skillman et al. 2011, 2013) would be also important to understand the statistical properties of the radio relics.

In contrast to giant radio relics, no prominent radio halo is found in CIZA J2242.8+5301 (van Weeren et al. 2010; Stroe et al. 2013) in the central region even at lower frequency 152MHz. That means that relativistic electrons are neither fully accelerated nor re-accelerated. For example, dying relativistic electrons escape from the backward side of the moving direction of radio relics, but are not re-accelerated by downstream turbulence. The fact leads to the condition

$$t_{\text{acc}} > \min\{t_{\text{cool}}, t_{\text{merger}}\}, \quad (1)$$

where t_{acc} , t_{cool} and t_{merger} are the acceleration timescale, the radiative cooling timescale and the merger time scale related to the particle acceleration, respectively. The Lorentz factor of relativistic electrons is $\gamma \sim 6.6 \times 10^3 \left(\frac{\nu(1+z)}{153\text{MHz}(1+0.192)} \right)^{1/2} \left(\frac{B}{1\mu\text{G}} \right)^{-1/2}$. Given the Lorentz factor, the cooling time of relativistic electrons is computed by the synchrotron and the inverse Compton losses, as follows,

$$t_{\text{cool}} \simeq 0.2 \left(\frac{\gamma}{6 \times 10^3} \right)^{-1} \times \left[\left(\frac{B}{1\mu\text{G}} \right)^2 + \left(\frac{B_{\text{CMB}}}{3.25(1+z)^2\mu\text{G}} \right)^2 \right]^{-1} \text{Gyr}, \quad (2)$$

where $B_{\text{CMB}}^2/(8\pi)$ is the energy density of the cosmic microwave background (CMB). We define the merger timescale, t_{merger} , as the time that the northern subhalo travels from the center-of-mass,

$$t_{\text{merger}} \simeq 0.2 \left(\frac{d_{\text{NM-CM}}}{440 h^{-1}\text{kpc}} \right) \left(\frac{v}{2000\text{km s}^{-1}} \right)^{-1} \text{Gyr}, \quad (3)$$

where we assume that the merging velocity $v = 2000 \text{ km s}^{-1}$ is equivalent to the shock velocity estimate by X-ray observation. We assume stochastic acceleration due to gyroresonant interaction with Alfvén waves (e.g. Ohno et al. 2002; Fujita et al. 2003; O’Sullivan et al. 2009), in the framework of the second-order Fermi acceleration. The acceleration timescale is computed by

$$t_{\text{acc}} \simeq \frac{K_g}{v_A^2}, \quad (4)$$

where v_A is the Alfvén velocity and $K_g \simeq cr_L/\xi_{\text{res}}$ is a spatial diffusion coefficient parallel to the mean magnetic field by a pitch angle scattering, respectively. Here, r_L is the Larmor radius and $\xi_{\text{res}} = (\delta B_{\text{res}}/B)^2$ is a fractional

energy of MHD turbulence at the wavelength satisfying a resonance scattering condition. For simplicity, we ignore the wave damping effect. The balance between the cooling time/merger time and the acceleration time constrains the fractional energy of the turbulence of

$$\xi_{\text{res}}^{\text{cool}} < 8 \times 10^{-7} \left(\frac{B}{1\mu\text{G}} \right)^{-4} \times \left[\left(\frac{B}{1\mu\text{G}} \right)^2 + \left(\frac{B_{\text{CMB}}}{3.25(1+z)^2\mu\text{G}} \right)^2 \right],$$

and

$$\xi_{\text{res}}^{\text{merger}} < 6 \times 10^{-7} \left(\frac{B}{1\mu\text{G}} \right)^{-7/2} \left(\frac{t_{\text{merger}}}{0.2\text{Gyr}} \right)^{-1}.$$

We here assume the electron density $n_e = 10^{-3} [\text{cm}^{-3}]$ and the mean molecular weight $\mu = 0.59$. The two constraints of $\xi_{\text{res}}^{\text{merger}}$ and $\xi_{\text{res}}^{\text{cool}}$ are comparable to each other. We note that the two equations above have different dependencies on the magnetic field strength, B . These constraints change slightly depending on the choice of the B -field strength. Although the exact limits would depend on the spatial position, our observations provide a crude upper limit on the fractional energy of the MHD turbulence as $\xi_{\text{res}} < \mathcal{O}(10^{-6})$. It indicates that the MHD turbulence is significantly suppressed in the central region, at this merging stage of the cluster. In the above discussion, we ignore the mechanism to generate the Alfvén waves. If the Alfvén waves is connected by the cascade of the fluid turbulence, the balance between the energy loss and gain ($t_{\text{acc}} = t_{\text{cool}}$) does not change but $t_{\text{acc}} = t_{\text{merger}}$ is modified to $t_{\text{acc}} + t_{\text{cas}} = t_{\text{merger}}$, where t_{cas} is the time scale of the cascade. As a result, the upper limit on $\xi_{\text{res}}^{\text{merger}}$ becomes larger than that on $\xi_{\text{res}}^{\text{cool}}$. We also note that the estimation of the MHD turbulence depends on the precise mechanisms of particle acceleration on the basis of microplasma physics, and thus further studies regarding other various mechanisms are essential for a deeper understanding of radio halos. If future deep radio observations discover very faint diffuse emission, the constrains on the MHD turbulence will be much improved.

We compare our weak-lensing masses with previous study (Jee et al. 2015). Jee et al. (2015) performed a weak-lensing mass estimate for the cluster using a color-magnitude selected galaxy sample that contains cluster red-sequence galaxies fainter than 22 ABmag. However, it has been well established by earlier work (e.g. Broadhurst et al. 2005; Okabe et al. 2013; Okabe & Smith 2015) that such a background selection can lead to systematic dilution of the weak-lensing signal, resulting in a substantial underestimate of the cluster mass especially at inner radii. By fixing the concentration parameter according to the mean c - M relation of Duffy et al. (2008) that is based on the WMAP five-year cosmology, they estimated $M_{200}^{\text{S}} = 6.9_{-1.8}^{+2.7} \times 10^{14} h^{-1} M_{\odot}$ and $M_{200}^{\text{N}} = 7.7_{-2.3}^{+2.6} \times 10^{14} h^{-1} M_{\odot}$ for the southern and northern halos, respectively. Their mass estimates for the northern and southern components, as well as their total mass estimate, are compatible with our results within large errors inherent in noisy

weak-lensing measurements with a small number of background galaxies. On the other hand, Jee et al. (2015) concluded that the cluster is the result of an equal-mass merger, whereas our best-fit model supports a $\sim 2:1$ ratio merger. In order to understand the origin of this discrepancy, we re-performed two-dimensional shear fitting assuming the single scaling concentration of Duffy et al. (2008) as done by Jee et al. (2015). We obtained $M_{200}^{\text{S}} = 8.1_{-4.1}^{+5.9} \times 10^{14} h^{-1} M_{\odot}$ and $M_{200}^{\text{N}} = 6.7_{-4.1}^{+7.3} \times 10^{14} h^{-1} M_{\odot}$ for the southern and northern halos, respectively. The resulting mass ratio is thus reduced to ~ 1.2 , in better agreement with their results. Therefore, their conclusions may be sensitive to the particular choice of the mean concentration-mass relation.

7. Summary

We have conducted weak-lensing analysis using three-band imaging of Subaru/Suprime-Cam. We have carefully selected background galaxy populations free of contamination by unlensed cluster galaxies, following the color-color selection method developed by (Medezinski et al. 2010). Two dimensional shear fitting enabled us to measure masses for two halos and their positions (Okabe et al. 2011). We have found that the southern halo is the main cluster and the northern halo is the colliding subcluster of which mass is about half of the main cluster mass. Spatial offsets between luminous galaxies and the weak-lensing-determined centers are at maximum 2σ level. The mass-to-light ratios for two halos within $250h_{70}^{-1}\text{kpc}$ from weak-lensing-determined centers are comparable because the concentration parameter for the subcluster is higher than that for the main cluster.

The distance ratio between outer edges of the two relics and the center of mass are comparable to those between two halo positions and the center of mass, as well as between the Mach numbers determined by X-ray observations. The gas halo is associated with the southern main halo, while no well-defined gas core is found in the northern subhalo. Our mass measurement could consistently explain the merger configuration observed by X-ray, radio and weak-lensing techniques. The result implies a possibility that the radio relic is formed after the core passage.

We have found that the curved shapes of radio relic coincides well with the projected mass distribution, indicating that radio relics on cluster-scale well follow the global structure of the mass distribution.

No prominent radio halo is found, which enabled us to put an upper limit of the fractional energy of MHD turbulence at resonant wavenumber of $(\delta B/B)^2 < \mathcal{O}(10^{-6})$, by comparing the acceleration timescale of the resonant acceleration with the cooling time or the merger time after the core passage.

Acknowledgments

We appreciate the anonymous referee for the helpful comments. We are grateful to N. Kaiser for developing the IMCAT package and making it publicly available. We

thank van Weeren R. J. for helpful discussion during his stay in Hiroshima University. This work was supported by “World Premier International Research Center Initiative (WPI Initiative)” and the Funds for the Development of Human Resources in Science and Technology under MEXT, Japan, and Core Research for Energetic Universe in Hiroshima University (the MEXT program for promoting the enhancement of research universities, Japan). N. Okabe is supported by a Grant-in-Aid from the Ministry of Education, Culture, Sports, Science, and Technology of Japan (26800097). H. Akamatsu is supported by a Grant-in-Aid for Japan Society for the Promotion of Science (JSPS) Fellows (26-606). Y.-Y. Zhang acknowledges support by the German BMWI through the Verbundforschung under grant 50 OR 1304. K. Umetsu acknowledges partial support from the Ministry of Science and Technology of Taiwan (grant MOST 103-2112-M-001-030-MY3).

References

- Akamatsu, H., & Kawahara, H. 2013, PASJ, 65, 16
 Akamatsu, H., van Weeren, R. J., Ogreaan, G. A., et al. 2015, ArXiv e-prints
 Bell, A. R. 1978, MNRAS, 182, 147
 Bhattacharya, S., Habib, S., Heitmann, K., & Vikhlinin, A. 2013, ApJ, 766, 32
 Blandford, R. D., & Ostriker, J. P. 1978, ApJ, 221, L29
 Broadhurst, T., Takada, M., Umetsu, K., et al. 2005, ApJ, 619, L143
 Brunetti, G., Blasi, P., Cassano, R., & Gabici, S. 2004, MNRAS, 350, 1174
 Brunetti, G., & Jones, T. W. 2014, International Journal of Modern Physics D, 23, 30007
 Brunetti, G., Giacintucci, S., Cassano, R., et al. 2008, Nature, 455, 944
 Drury, L. O. 1983, Reports on Progress in Physics, 46, 973
 Duffy, A. R., Schaye, J., Kay, S. T., & Dalla Vecchia, C. 2008, MNRAS, 390, L64
 Enßlin, T. A., & Gopal-Krishna. 2001, A&A, 366, 26
 Feretti, L., Giovannini, G., Govoni, F., & Murgia, M. 2012, A&A Rev., 20, 54
 Finoguenov, A., Sarazin, C. L., Nakazawa, K., Wik, D. R., & Clarke, T. E. 2010, ApJ, 715, 1143
 Fujita, Y., Takizawa, M., & Sarazin, C. L. 2003, ApJ, 584, 190
 Govoni, F., Markevitch, M., Vikhlinin, A., et al. 2004, ApJ, 605, 695
 Hoeft, M., Brüggen, M., & Yepes, G. 2004, MNRAS, 347, 389
 Ilbert, O., McCracken, H. J., Le Fèvre, O., et al. 2013, A&A, 556, A55
 Jee, M. J., Stroe, A., Dawson, W., et al. 2015, ApJ, 802, 46
 Kaiser, N., Squires, G., & Broadhurst, T. 1995, ApJ, 449, 460
 Loken, C., Roettiger, K., Burns, J. O., & Norman, M. 1995, ApJ, 445, 80
 Markevitch, M., Govoni, F., Brunetti, G., & Jerius, D. 2005, ApJ, 627, 733
 Medezinski, E., Broadhurst, T., Umetsu, K., et al. 2010, MNRAS, 405, 257
 Medezinski, E., Umetsu, K., Okabe, N., et al. 2015, ArXiv e-prints
 Merluzzi, P., Busarello, G., Haines, C. P., et al. 2015, MNRAS, 446, 803
 Miyazaki, S., Komiyama, Y., Sekiguchi, M., et al. 2002, PASJ, 54, 833
 Nakazawa, K., Sarazin, C. L., Kawaharada, M., et al. 2009, PASJ, 61, 339
 Navarro, J. F., Frenk, C. S., & White, S. D. M. 1996, ApJ, 462, 563
 Ogreaan, G. A., Brüggen, M., van Weeren, R., et al. 2014, MNRAS, 440, 3416
 Oguri, M., Takada, M., Okabe, N., & Smith, G. P. 2010, MNRAS, 405, 2215
 Ohno, H., Takizawa, M., & Shibata, S. 2002, ApJ, 577, 658
 Okabe, N., Bourdin, H., Mazzotta, P., & Maurogordato, S. 2011, ApJ, 741, 116
 Okabe, N., Futamase, T., Kajisawa, M., & Kuroshima, R. 2014a, ApJ, 784, 90
 Okabe, N., & Smith, G. P. 2015, ArXiv e-prints
 Okabe, N., Smith, G. P., Umetsu, K., Takada, M., & Futamase, T. 2013, ApJ, 769, L35
 Okabe, N., Takada, M., Umetsu, K., Futamase, T., & Smith, G. P. 2010, PASJ, 62, 811
 Okabe, N., & Umetsu, K. 2008, PASJ, 60, 345
 Okabe, N., Umetsu, K., Tamura, T., et al. 2014b, PASJ, 66, 99
 O’Sullivan, S., Reville, B., & Taylor, A. M. 2009, MNRAS, 400, 248
 Ouchi, M., Shimasaku, K., Okamura, S., et al. 2004, ApJ, 611, 685
 Popesso, P., Böhringer, H., Romaniello, M., & Voges, W. 2005, A&A, 433, 415
 Roettiger, K., Burns, J. O., & Stone, J. M. 1999, ApJ, 518, 603
 Schlafly, E. F., & Finkbeiner, D. P. 2011, ApJ, 737, 103
 Schlickeiser, R., Sievers, A., & Thiemann, H. 1987, A&A, 182, 21
 Skillman, S. W., Hallman, E. J., O’Shea, B. W., et al. 2011, ApJ, 735, 96
 Skillman, S. W., Xu, H., Hallman, E. J., et al. 2013, ApJ, 765, 21
 Stroe, A., Harwood, J. J., Harcastle, M. J., & Röttgering, H. J. A. 2014, MNRAS, 445, 1213
 Stroe, A., van Weeren, R. J., Intema, H. T., et al. 2013, A&A, 555, A110
 Tormen, G., Moscardini, L., & Yoshida, N. 2004, MNRAS, 350, 1397
 Umetsu, K., Medezinski, E., Broadhurst, T., et al. 2010, ApJ, 714, 1470
 Umetsu, K., Zitrin, A., Gruen, D., et al. 2015, ArXiv e-prints
 Umetsu, K., Medezinski, E., Nonino, M., et al. 2014, ApJ, 795, 163

- van Weeren, R. J., Brüggen, M., Röttgering, H. J. A., & Hoeft, M. 2011, MNRAS, 418, 230
- van Weeren, R. J., Röttgering, H. J. A., Brüggen, M., & Hoeft, M. 2010, Science, 330, 347
- Watanabe, E., Takizawa, M., Nakazawa, K., et al. 2011, PASJ, 63, 357
- Yagi, M., Kashikawa, N., Sekiguchi, M., et al. 2002, AJ, 123, 66
- Yang, X., Mo, H. J., van den Bosch, F. C., et al. 2006, MNRAS, 373, 1159